

Non-Negative Matrix Factorization for 2D-XAS Images of Lithium Ion Batteries

Hiroki Tanimoto, Xu Hongkun, and Toru Aonishi*

School of Computing, Tokyo Institute of Technology

Masaishiro Mizumaki

Japan Synchrotron Radiation Research Institute

Yoshiki Seno

Saga Prefectural Regional Industry Support Center

Yuta Kimura and Koji Amezawa

Institute of Multidisciplinary Research for Advanced Materials, Tohoku University

Ichiro Akai

Institute of Industrial Nanomaterials, Kumamoto University

(Dated: October 12, 2020)

Abstract

Lithium ion batteries are used in a wide range of fields such as mobile devices, electric vehicles, and energy storage systems for renewable energy. Because high power output and rapid charging are required for progress in such applications, there is a demand for the performance rate to be increased. Lithium ion batteries experience a spatially non-uniform reaction during charging and discharging. The consequent non-uniform spatial domain structure and its physical properties are not completely understood. In this paper, we develop a machine learning method that automatically extracts spatial domains with different absorption spectra profiles from Co K-edge two-dimensional X-ray absorption spectroscopy (2D-XAS) images of lithium ion batteries. The method decomposes the 2D-XAS data into spatial domains and their corresponding absorption spectra by using modified orthogonal non-negative matrix factorization and removal of the common background signal. We conducted experiments showing that some of the extracted factors represent physically interpretable information on the state of charge.

*Electronic address: aonishi@c.titech.ac.jp

I. INTRODUCTION

Lithium ion batteries are candidates for high-capacity and high-power electric storage systems in a wide range of fields, such as mobile devices, electric vehicles and energy storage systems for renewable energy. Because high power output and rapid charging are required for progress in such applications, there is a demand for higher performance rates[1–4]. However, the present lithium ion batteries have poor performance and stability under high rate conditions[2–4]. One of the reasons is that they experience spatially non-uniform reactions during charging and discharging. To improve high-rate performance, it is essential to understand the mechanism and the governing factors of the reaction inhomogeneity[5–16].

To visualize the reaction inhomogeneity, Nakamura et al. sought to image the state of charge (SOC) of Li_xCoO_2 in a model composite electrode by using two-dimensional X-ray absorption spectroscopy (2D-XAS) [17]. They two-dimensionally acquired Co-K-edge X-ray absorption spectra of Li_xCoO_2 at various positions of a model composite electrode. Then, they determined the peak top energy from the acquired spectra and made a two-dimensional map of the SOC in the model electrode by using the one-to-one relation between the peak top energy and the SOC of Li_xCoO_2 determined from reference materials with well-defined SOC values. Through visualization of the reaction inhomogeneity, they showed that the electrochemically active region decreases with increasing current density during charging.

The SOC of Li_xCoO_2 is an important physical factor affecting the uniformity of electrochemical reactions, but other factors could also contribute to the reaction inhomogeneity. Here, XAS data give not only the SOC but also other information on local structures on the atomic scale, the electron spin states, and so on[18–22]. To better understand the mechanism and the governing factors of the reaction inhomogeneity, we need to distinguish individual spatial domains that otherwise share physical properties not limited to the SOC. The aim of this study was thus to develop a machine learning method that automatically extracts spatial domains with different profiles of absorption spectra from 2D-XAS data on the model composite electrode measured by Nakamura et al. (2017) [17].

Shiga et al. applied non-negative matrix factorization (NMF) [23] to scanning transmission electron microscopy (STEM) - electron energy-loss spectroscopy (EELS) / energy-dispersive X-ray (EDX) spectral datasets acquired from well-defined reference materials and successfully extracted individual domains with different components [24, 25]. Furthermore,

the NMF method proposed by Shiga et al. has been applied to analyses of STEM-EELS and Raman datasets of lithium ion battery electrolyte material [26–28]. The profiles of STEM and Raman spectra were markedly different depending on the dominant components. However, the XAS spectra of the model composite electrode measured by Nakamura et al. (2017) varied very little from one position to another because the spectra had a common background signal (see Fig. 1 in [17]). As mentioned in Maruyama et al. (2014) [29], the common background signal is harmful to NMF. That is, it is difficult to use NMF to factorize 2D-XAS data of the model composite electrode unless the common background signal can be removed.

In this study, to remove the common background signal from the 2D-XAS data of the model composite electrode, we obtained difference spectra by subtracting X-ray absorption spectrum of the $\text{Li}_{0.5}\text{CoO}_2$ reference material from 2D-XAS data in a preprocessing step and then applied a modified orthogonal NMF (ONMF) to the difference spectra [30, 31]. The modified ONMF we propose here imposes column orthogonality on one side’s nonnegative factor matrix representing spatial domain structures, but it relaxes the non-negativity restriction on the other side’s factor matrix representing the spectra because the difference spectra take signed real values. Furthermore, we estimated the number of spatial domains with different spectral profiles by determining the rank of the factor matrices of the modified ONMF using bi-cross-validation [32]. After decomposing the 2D-XAS data into spatial domains and their corresponding spectra, we can identify the physical properties and features from the separated X-ray absorption spectra of the individual domains by using, e.g., Bayesian spectroscopy [33–35]. Hence, this development gives us a means to gain a better understanding of the physical factors for governing electrochemical reaction inhomogeneity in the near future.

The main contribution of this study is the automatic domain extraction method that can identify and distinguish very small differences in X-ray absorption spectra at all positions. We assessed the performance of our method on synthetic data that mimic profiles of X-ray absorption spectra and confirmed that the ground-truth domains of the synthetic data were correctly detected and the correct number of ground-truth domains was obtained. Then, we determined the number of spatial domains with different spectral profiles from real 2D-XAS data of a model composite electrode and extracted spatial domain patterns from the real data. The extracted spatial domains were highly correlated with ones obtained with the

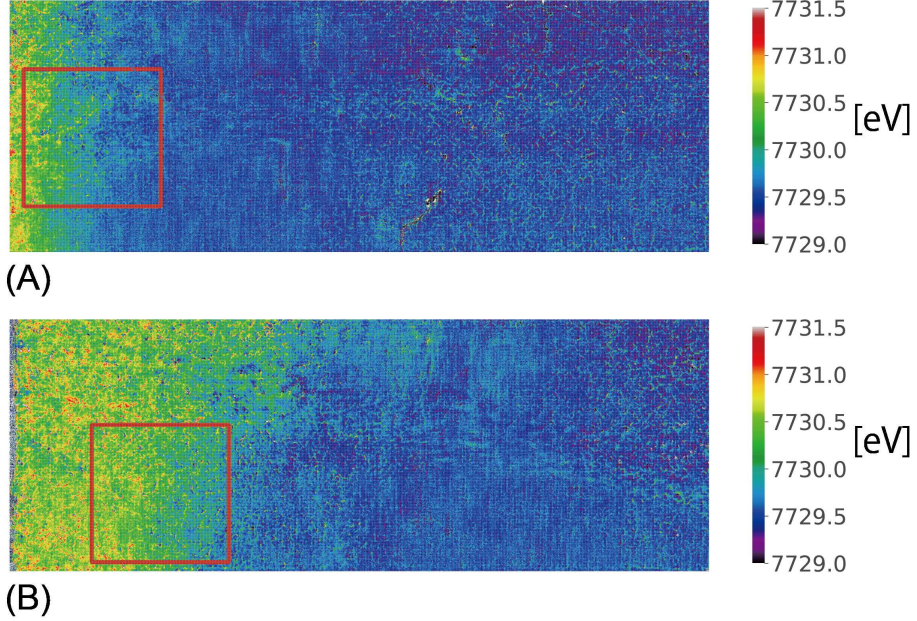


FIG. 1: 2D-XAS data of Co K-edge X-ray absorption spectra of Li_xCoO_2 of the model composite electrode. Two data sets shown in this figure consist of 100 frames (corresponding to an energy range from 7700 to 7740 eV) of 550×1530 pixels (corresponding to an area of about $1100 \times 3060 \mu\text{m}$). (A) Two-dimensional map of the peak top energy obtained from data after charging model electrode to 4.2 V at a current rate of 12 mAcm^{-2} . (B) Two-dimensional map of the peak top energy obtained from the data after charging model electrode to 4.2 V with current rate of 9 mAcm^{-2} . The two datasets were 300×300 pixels (corresponding to area of about $600 \times 600 \mu\text{m}$) clipped from the two whole images, as shown by the red rectangles in (A) and (B).

k-means method; they were also correlated with patterns obtained by thresholding the peak top energy of the X-ray absorption spectra, which reflect the spatial distribution of the SOC of Li_xCoO_2 .

II. MATERIALS AND METHODS

A. Data and preprocessing

The data acquired in Nakamura et al. (2017) [17] were provided by coauthorss of this paper. They two-dimensionally observed the change of Co-K-edge X-ray absorption spectra

of Li_xCoO_2 of the model composite electrode. The XAS measurements at the Co K edge were carried out at the beamlines of BL01B1 and BL28XU in SPring-8, Japan. Figures 1 (A) and (B) show two-dimensional maps of the peak top energy obtained from the data used in this study. An area of about $1100 \times 3060 \mu\text{m}$ was observed with a spatial resolution of approximately $2 \mu\text{m}$ in an energy range from 7700 to 7740 eV at energy steps of 0.4 eV. The model electrode was charged to 4.2 V at current rates of 9 mA cm^{-2} (Fig. 1 (B)) and 12 mA cm^{-2} (Fig. 1 (A)). The procedure for fabricating the model electrode and the details of the experiments are given in the papers [16, 17]. The two 2D-XAS datasets we analyzed consisted of 100 frames (corresponding to an energy range from 7700 to 7740 eV) of 300×300 pixels (corresponding to area of about $600 \times 600 \mu\text{m}$), which were clipped from the two whole images, as shown by the red rectangles in Figs. 1 (A) and (B).

In the preprocessing, we normalized each Co K-edge X-ray absorption spectrum at each pixel point to be zero at 7700 eV and one at 7740 eV. Then, we reshaped the 2D array of pixels into a 1D column of pixels for each frame and thereby obtained a 90000 by 100 spectrum matrix \mathbf{X}_0 . As described in the Introduction, the X-ray absorption spectra acquired from the model electrode have a large common background signal and vary only a little from one position to another. To enhance the differences in the absorption spectra, we subtracted the X-ray absorption spectrum of $\text{Li}_{0.5}\text{CoO}_2$ reference material from the spectrum matrix \mathbf{X}_0 :

$$\mathbf{X} = \mathbf{X}_0 - \mathbf{1}\mathbf{b}, \quad (1)$$

where $\mathbf{1}$ is a 90000-dimensional column vector in which all the elements are 1, and \mathbf{b} is a 100-dimensional row vector storing the X-ray absorption spectrum of the $\text{Li}_{0.5}\text{CoO}_2$ reference material. The matrix \mathbf{X} obtained by this subtraction is called the difference spectrum matrix. The spectrum matrix \mathbf{X}_0 is non-negative, whereas the difference spectrum matrix \mathbf{X} takes signed values due to the subtraction in Eq. (1).

B. Modified ONMF for 2D-XAS images

We assume that the difference spectrum matrix \mathbf{X} can be factorized into a real non-negative matrix $\mathbf{W} \in \mathbb{R}_+^{m \times r}$ and a real signed matrix $\mathbf{H} \in \mathbb{R}^{n \times r}$ whose rank is equal to $r < \min(m, n)$. Under this assumption, we introduce the following generative model for \mathbf{X} ,

$$\mathbf{X} = \mathbf{W}\mathbf{H}^T + \boldsymbol{\varepsilon}, \quad (2)$$

where all elements of $\boldsymbol{\varepsilon} \in \mathbb{R}^{m \times n}$ are independent and identically distributed (i.i.d.) Gaussian noise. Each column vector of \mathbf{W} , denoted as $\mathbf{w}_k \in \mathbb{R}_+^{m \times 1}$, represents the k -th spatial domain ($k \in \{1, \dots, r\}$), and each column vector of \mathbf{H} , denoted as $\mathbf{h}_k \in \mathbb{R}^{n \times 1}$, represents the k -th difference spectrum corresponding to the k -th spatial domain ($k \in \{1, \dots, r\}$). To represent the difference spectrum taking signed values due to the subtraction in Eq (1), each element of \mathbf{h}_k is defined as a signed real value. Using these column and row vectors, the generative model of Eq. (2) can be rewritten as

$$\mathbf{X} = \sum_{k=1}^r \mathbf{w}_k \mathbf{h}_k^T + \boldsymbol{\varepsilon}. \quad (3)$$

Under the i.i.d. Gaussian noise assumption in Eq. (2), \mathbf{W} and \mathbf{H} can be estimated by minimizing the following objective function,

$$J = \|\mathbf{X} - \mathbf{W}\mathbf{H}^T\|_2^2, \quad (4)$$

where $\|\mathbf{X}\|_2$ denotes the Frobenius norm.

We seek to minimize the objective function defined in Eq. (4) by imposing column orthogonality on \mathbf{W} and using an algorithm based on the hierarchical alternating least squares (HALS) algorithm for ONMF proposed by Kimura et al. (2009) [31]. We summarize this ONMF algorithm below.

The HALS algorithm minimizes the objective function defined in Eq. (4) alternatively with respect to each pair of column vector \mathbf{w}_k and row vector \mathbf{h}_k in \mathbf{W} and \mathbf{H} while keeping the other vectors fixed [36]. Each alternating minimization with respect to \mathbf{w}_k and \mathbf{h}_k can be equivalently formulated as a minimization of the following objective function,

$$J_k = \|\mathbf{X}^{(k)} - \mathbf{w}_k \mathbf{h}_k^T\|_2^2, \quad (5)$$

$$\mathbf{X}^{(k)} = \mathbf{X} - \sum_{k'(\neq k)} \mathbf{w}_{k'} \mathbf{h}_{k'}^T, \quad (6)$$

where $\mathbf{X}^{(k)}$ denotes the residual between the data \mathbf{X} and the factorization result excluding the k -th factor $\mathbf{w}_k \mathbf{h}_k^T$.

Kimura et al. (2010) formulated an optimization problem that minimizes J_k subject to the following constraint for imposing column orthogonality on one side's nonnegative factor matrix [31]:

$$\mathbf{W}^{(k)T} \mathbf{w}_k = \sum_{k'(\neq k)} \mathbf{w}_{k'}^T \mathbf{w}_k = 0, \quad (7)$$

where $\mathbf{W}^{(k)}$ denotes the sum of all column vectors in \mathbf{W} excluding the k -th column vector \mathbf{w}_k . To solve this optimization problem, they introduced the following Lagrange function with Lagrange multiplier λ_k ,

$$L_k = \|\mathbf{X}^{(k)} - \mathbf{w}_k \mathbf{h}_k^T\|_2^2 + \lambda_k (\mathbf{W}^{(k)T} \mathbf{w}_k). \quad (8)$$

Then, they found the stationary points at which the first partial derivatives of L_k with respect to \mathbf{w}_k and \mathbf{h}_k are zero and obtained an update rule of HALS algorithm for ONMF.

The modified ONMF we use here imposes column orthogonality on nonnegative \mathbf{W} , but relaxes the non-negativity restriction on \mathbf{H} . To represent the difference spectrum taking signed values, each element of \mathbf{h}_k is defined as a real signed value. This is a point of difference from the HALS algorithm proposed by Kimura et al. In this case, the HALS algorithm for the modified ONMF is given by the following alternating update equation:

$$\mathbf{w}_k \leftarrow [\mathbf{X}^{(k)} \mathbf{h}_k - \frac{\mathbf{W}^{(k)T} \mathbf{X}^{(k)} \mathbf{h}_k}{\mathbf{W}^{(k)T} \mathbf{W}^{(k)}} \mathbf{W}^{(k)}]_+, \quad (9)$$

$$\mathbf{h}_k \leftarrow \mathbf{X}^{(k)T} \mathbf{w}_k, \quad (10)$$

where $[\cdot]_+$ denotes half-wave rectification $[x]_+ = \max(x, 0)$ resulting in a nonnegative \mathbf{w}_k . Note that there is no such half-wave rectification on \mathbf{h}_k , which is different from the HALS algorithm proposed by Kimura et al. [31].

Since $\mathbf{X}^{(k)} = \mathbf{X} - \sum_{k'(\neq k)} \mathbf{w}_{k'} \mathbf{h}_{k'} = \mathbf{X} - \mathbf{W} \mathbf{H} + \mathbf{w}_k \mathbf{h}_k$, the above alternating update equation can be rewritten in an easily implementable form:

$$\mathbf{w}_k \leftarrow [\mathbf{u} - \frac{\mathbf{W}^{(k)T} \mathbf{u}}{\mathbf{W}^{(k)T} \mathbf{W}^{(k)}} \mathbf{W}^{(k)}]_+, \quad (11)$$

$$\mathbf{h}_k \leftarrow (\mathbf{X}^T \mathbf{W})_k - \mathbf{H}(\mathbf{W}^T \mathbf{W})_k + \mathbf{h}_k \mathbf{w}_k^T \mathbf{w}_k, \quad (12)$$

where $\mathbf{u} = (\mathbf{X} \mathbf{H})_k - \mathbf{W}(\mathbf{H}^T \mathbf{H})_k + \mathbf{w}_k \mathbf{h}_k^T \mathbf{h}_k$. Algorithm 1 is the HALS algorithm for the modified ONMF.

In the numerical experiments reported below, the HALS algorithm was repeated under the same conditions five times with different randomly generated initial values, and the solution with the smallest value of the objective function was selected from the five trials. Because of the column orthogonality $\mathbf{W}^T \mathbf{W} \simeq \mathbf{I}$, we approximately obtained the X-ray absorption spectra of the individual domains by calculating $\mathbf{W}^T \mathbf{X}_0$.

Algorithm 1 HALS algorithm for modified ONMF

```

1: Initialize  $\mathbf{W}$  and  $\mathbf{H}$  randomly.
2:  $\mathbf{U} = \mathbf{W}\mathbf{1}_r$ 
3: while Convergence criterion is not satisfied do
4:    $\mathbf{A} = \mathbf{X}\mathbf{H}$ 
5:    $\mathbf{B} = \mathbf{H}^T\mathbf{H}$ 
6:   for  $k=1$  to  $r$  do
7:      $\mathbf{W}^{(k)} = \mathbf{U} - \mathbf{w}_k$ 
8:      $u = \mathbf{A}_{:k} - \mathbf{W}\mathbf{B}_{:k} + \mathbf{B}_{kk}\mathbf{w}_k$ 
9:      $\mathbf{w}_k = [\mathbf{u} - \frac{\mathbf{W}^{(k)T}\mathbf{u}}{\mathbf{W}^{(k)T}\mathbf{W}^{(k)}}\mathbf{W}^{(k)}]_+$ 
10:     $\mathbf{w}_k = \mathbf{w}_k/||\mathbf{w}_k||^2$ 
11:     $\mathbf{U} = \mathbf{W}^{(k)} + \mathbf{w}_k$ 
12:   end for
13:    $\mathbf{C} = \mathbf{W}^T\mathbf{X}$ 
14:    $\mathbf{D} = \mathbf{W}^T\mathbf{W}$ 
15:   for  $k=1$  to  $r$  do
16:      $\mathbf{h}_k = \mathbf{C}_{:k} - \mathbf{H}\mathbf{D}_{:k} + \mathbf{D}_{kk}\mathbf{h}_k$ 
17:   end for
18: end while

```

C. Bi-Cross Validation for model selection

We seek to estimate the number of spatial domains with different spectral profiles by applying model selection to the modified ONMF. Here, we can use bi-cross-validation [32] to determine the rank of the two factor matrices r from the data X . Bi-cross-validation is applicable to a wide class of matrix factorization methods [32].

The data $\mathbf{X} \in \mathbb{R}^{m \times n}$ is separated into four blocks consisting of $\mathbf{X}_A, \mathbf{X}_B, \mathbf{X}_C$ and \mathbf{X}_D as follows,

$$\mathbf{X} = \begin{pmatrix} \mathbf{X}_A & \mathbf{X}_B \\ \mathbf{X}_C & \mathbf{X}_D \end{pmatrix}. \quad (13)$$

Let \mathbf{X}_D be factorized into \mathbf{W}_D and \mathbf{H}_D by applying the HALS algorithm described above. The estimated value of the denoised \mathbf{X}_D becomes $\hat{\mathbf{X}}_D = \mathbf{W}_D\mathbf{H}_D^T$. As reported in [32], the

generalization error can be measured from a residual defined by $\hat{\boldsymbol{\varepsilon}}_A = \mathbf{X}_A - \mathbf{X}_B \hat{\mathbf{X}}_D^+ \mathbf{X}_C$, where $\hat{\mathbf{X}}_D^+$ is the pseudo-inverse of $\hat{\mathbf{X}}_D$.

The detailed procedure for calculating the cross-validation error is as follows. Every 20th row and column vectors are selected from \mathbf{X} . The partial blocks \mathbf{X}_A , \mathbf{X}_B , \mathbf{X}_C and \mathbf{X}_D are organized with these picked vectors and the remaining row and column vectors. Then, \mathbf{X}_D is factorized into \mathbf{W}_D and \mathbf{H}_D by the HALS described above, and the generalization error $\|\hat{\boldsymbol{\varepsilon}}_A\|_2^2$ is calculated. This process is repeated 20 times until all row and column vectors have been picked, and the mean of $\|\hat{\boldsymbol{\varepsilon}}_A\|_2^2$ is obtained. Hereafter, the mean of $\|\hat{\boldsymbol{\varepsilon}}_A\|_2^2$ is called the bi-cross-validation error. In the numerical experiments, the bi-cross-validation error under the same conditions was calculated five times with different randomly generated initial values, and the rank of the two factor matrices r was determined by searching for the minimum point of the average bi-cross-validation error excluding outliers from the five trials.

D. Synthetic data

We generated synthetic data as ground truth on which we could objectively assess the performance of our method.

We created eight separate domains by hand on a 400×400 pixel image (Fig. 2(A)) and stored them as a 160000 by 8 matrix \mathbf{W}_g by reshaping the 2D pixel array into a 1D array. We synthesized eight different spectra on a 100 by 8 matrix \mathbf{H}_g , in which each consisted of a randomly shifted single error function and two Gaussians to mimic profiles of X-ray absorption spectra (Fig. 2(B)). Then, we obtained a 160000 by 100 synthetic spectrum matrix X_0 by multiplying \mathbf{W}_g and \mathbf{H}_g^T . We also created a spectrum mimicking the X-ray absorption spectrum of $\text{Li}_{0.5}\text{CoO}_2$ reference material in the same manner.

E. k-means method

To confirm the consistency of the results obtained with the modified ONMF and other methods, we used the k-means method to analyze the 2D-XAS data and compared its results with those of our method. The k-means method is a standard clustering method that classifies data into k clusters. To extract individual spatial domains with different

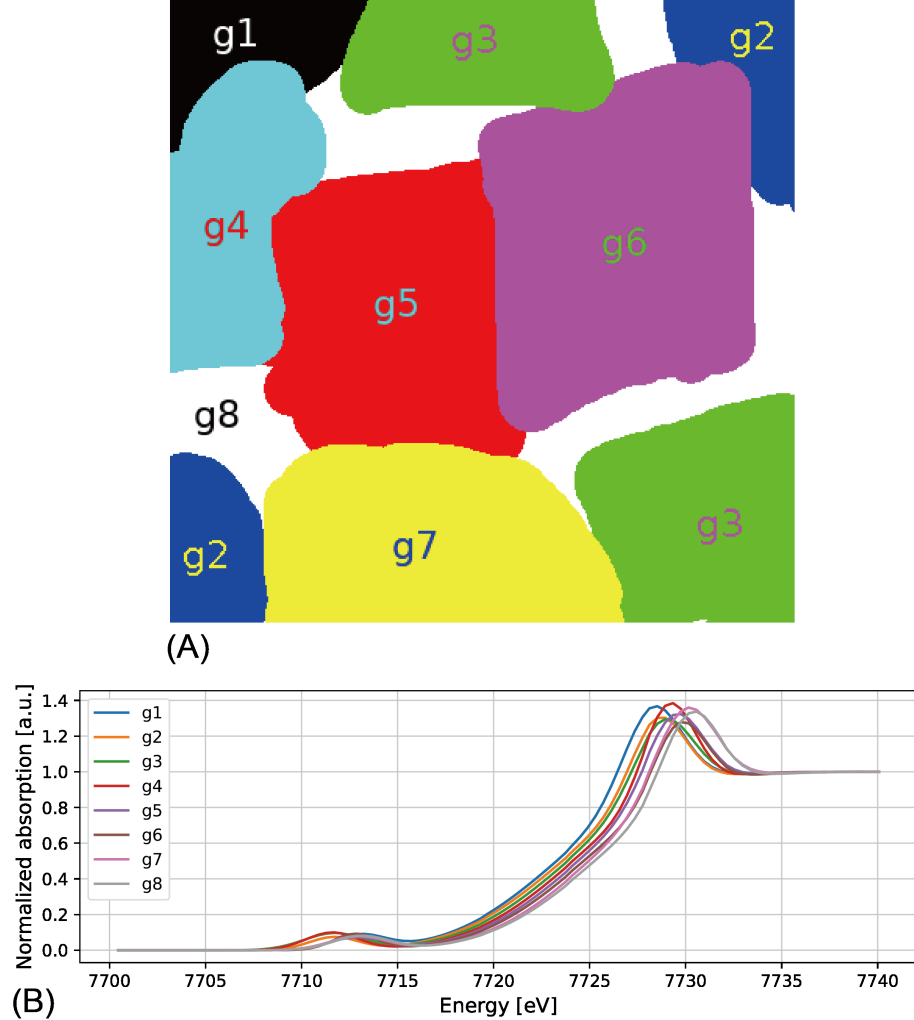


FIG. 2: Synthetic data. (a) Eight separate domains g_1 – g_8 drawn by hand. (b) Eight different spectra g_1 – g_8 mimicking profiles of X-ray absorption spectra.

spectral profiles, the k-means method is formulated as the following optimization problem [37].

$$\min_{\{\mathbf{h}_j\}, \{w_{ij}\}} \sum_{i=1}^m \sum_{j=1}^r w_{ij} \|\mathbf{x}_i - \mathbf{h}_j\|_2^2, \quad (14)$$

where \mathbf{x}_i is the X-ray absorption spectrum at the i -th pixel, and \mathbf{h}_j denotes the mean absorption spectrum of the j -th domain. w_{ij} is a one-hot representation that takes either 1 or 0 depending on whether or not \mathbf{x}_i belongs to the j -th domain. The vector denoted by $\mathbf{w}_i^{k\text{-means}}$ represents the spatial structure of the i -th domain.

To quantitatively compare results obtained with the modified ONMF and those with the k-means method, we calculated the cross correlation of all combinations of $\mathbf{w}_{i'}$ of the

modified ONMF and $\mathbf{w}_i^{k-means}$,

$$\text{Corr}_{i',i} = \frac{\mathbf{w}_{i'}^T \mathbf{w}_i^{k-means}}{\sqrt{\|\mathbf{w}_{i'}\|_2 \|\mathbf{w}_i^{k-means}\|_2}}. \quad (15)$$

F. Peak top energy

To visualize the reaction inhomogeneity, Nakamura et al. obtained two-dimensional maps of SOC of Li_xCoO_2 in the model composite electrode from the peak top energy of the X-ray absorption spectrum at each pixel [17]. To confirm the consistency of the results obtained with the modified ONMF and those with the peak top energy, we compared the spatial structures obtained with these two methods.

First, we determined the peak top energy by fitting a Gaussian distribution to the X-ray absorption spectrum at each pixel and obtained two-dimensional maps of the peak top energy. Next, we classified pixels on the obtained map into three sets, denoted by D1, D2 and D3, which have the peak top energies in the ranges of (E_2, ∞) , (E_2, E_1) and $(0, E_1)$, respectively. E_1 and E_2 are thresholds for classifying all of the pixels into D1, D2, or D3.

To quantitatively compare results obtained with the modified ONMF and those with the peak top energy, we calculated the cross correlation of \mathbf{w}_i of the modified ONMF and pixels of Dk using Eq. (15). In this comparison, the threshold E_1 was determined by maximizing the cross correlation between the pixels of D3 and the most similar \mathbf{w}_i to the pixels of D3, while the threshold E_2 was determined by maximizing the cross correlation between the pixels of D1 and the most similar \mathbf{w}_i to the pixels of D1.

Furthermore, to confirm the consistency between results obtained with the modified ONMF and with respect to the peak top energy, we also compared the relative relations of the peak top energies of the three domains of the modified ONMF that are most highly correlated with D1, D2 and D3 with the thresholds E_1 and E_2 .

III. RESULTS

A. Performance evaluation using synthetic data

We assessed the performance of our method on synthetic data with eight separate domains.

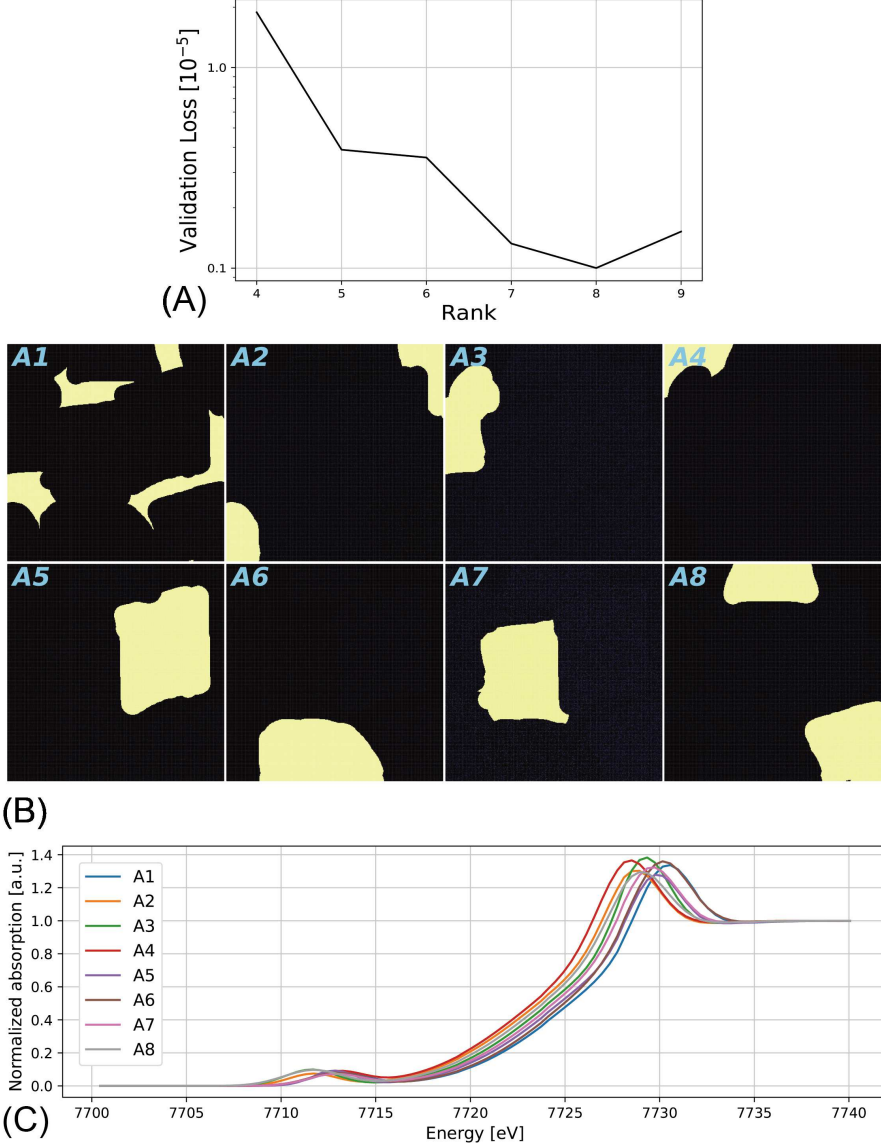


FIG. 3: Performance evaluation of modified ONMF on synthetic data. (A) Bi-cross-validation error as a function of rank r for $4 \leq r \leq 9$. (B) Eight spatial domains A1–A8 factorized by modified ONMF. (C) Absorption spectra corresponding to domains A1–A8.

First, the rank of the factor matrices r was determined by bi-cross-validation. Figure 3(A) shows the bi-cross-validation error as a function of the rank r for $4 \leq r \leq 9$. The bi-cross-validation error was minimized at $r = 8$, and thus, the estimated rank was confirmed to be identical to the number of ground-truth domains of synthetic data.

When the rank of the factor matrices was set to eight ($r = 8$), the modified ONMF successfully extracted eight spatial domains with different spectral profiles from the synthetic

data (Figs. 3(B) and (C)). A1–A8 in Figs. 3(B) show spatial domain patterns obtained by reshaping the column vectors of the factorized matrix \mathbf{W} into 2D arrays, and A1–A8 in Figs. 3(C) indicate the absorption spectra corresponding to domains A1–A8 in Figs. 3. Note that because of the column orthogonality on \mathbf{W} , the absorption spectra corresponding to domains A1–A8 can be approximately obtained by calculating $\mathbf{W}^T \mathbf{X}_0$. A comparison of A1–A8 in Fig. 3 and g1–g8 in Fig. 2 confirmed that the spatial domains obtained by our method were identical with the ground-truth domains g1–g8 in the synthetic data.

B. Analyses of real 2D-XAS data

By using the modified ONMF and removing the common background signal from the real 2D-XAS data of the model composite electrode, we sought to extract spatial domains with different spectral profiles. Here, we acquired two data sets for the model electrode charged to 4.2 V at current rates of 9 mA cm^{-2} (Fig. 1 (B)) and 12 mA cm^{-2} (Fig. 1 (A)) from Nakamura et al. (2017) [17]. To reduce the calculation time, we clipped data from the whole images, as indicated by the rectangles in Figs. 1 (A) and (B).

First, the rank of the factor matrices r was determined by bi-cross-validation. Figures 4(A) and 5(A) show the bi-cross-validation error as a function of the rank r for $7 \leq r \leq 11$. The bi-cross-validation errors were minimized at $r = 10$ on both data.

Next, we examined how our method decomposed the 2D-XAS data into spatial domains and their corresponding absorption spectra when the rank of the factor matrices was set to ten ($r = 10$) (Figs. 4 and 5). B1–B10 in Figs. 4(B) and 5(B) show spatial domain patterns obtained by reshaping the column vectors of the factorized matrix \mathbf{W} , and B1–B10 in Figs. 4(C) and 5(C) indicate absorption spectra corresponding to the ten domains B1–B10 in Figs. 4(B) and 5(B). Note that because of the column orthogonality of \mathbf{W} , the absorption spectra corresponding to domains B1–B10 can be approximately obtained by calculating $\mathbf{W}^T \mathbf{X}_0$.

Thus, we confirmed that our method could determine the rank of the factor matrices r and extract spatial domains with different spectral profiles from different real 2D-XAS data.

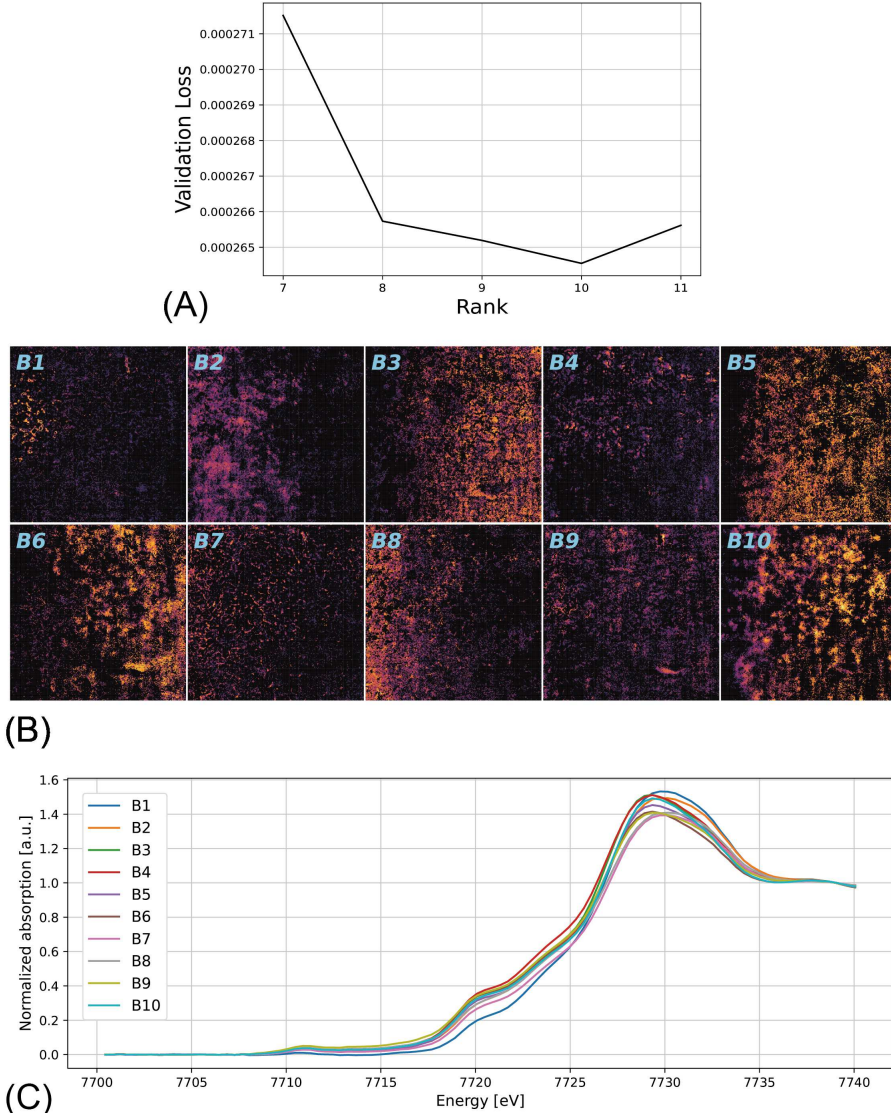


FIG. 4: Extraction of spatial domains and spectra using modified ONMF in combination with removal of common background signal from real 2D-XAS data of model electrode charged to 4.2 V at current rate of 12 mA cm^{-2} in Fig. 1(A). (A) Bi-cross-validation error as a function of rank r for $7 \leq r \leq 11$. (B) Ten spatial domains B1–B10 factorized by the modified ONMF. (C) Absorption spectra corresponding to domains B1–B10.

C. Comparison with k-means method

To confirm the consistency of the results obtained with the modified ONMF and the other methods, the k-means method was used to classify real 2D-XAS data into several clusters.

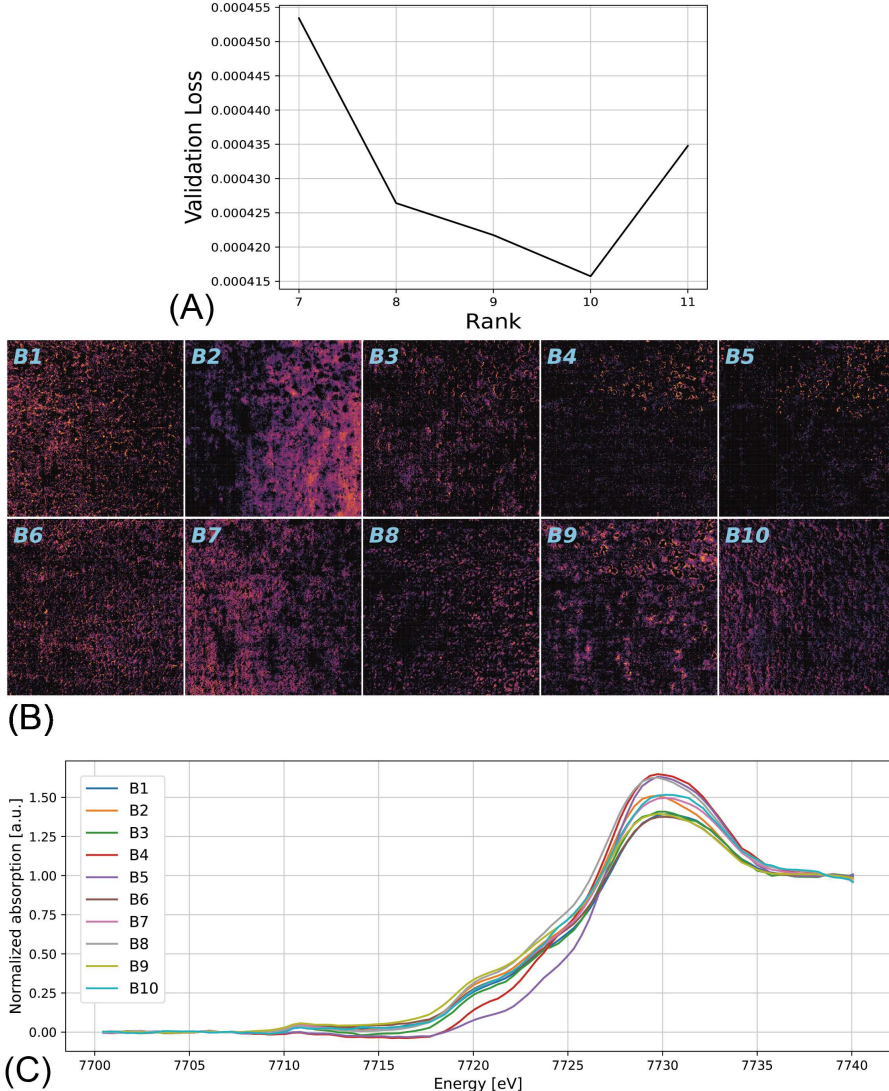


FIG. 5: Extraction of spatial domains and spectra using modified ONMF in combination with removal of common background signal from real 2D-XAS data of model electrode charged to 4.2 V at current rate of 9 mA cm^{-2} in Fig. 1(B). (A) Bi-cross-validation error as a function of rank r for $7 \leq r \leq 11$. (B) Ten spatial domains B1–B10 factorized by the modified ONMF. (C) Absorption spectra corresponding to domains B1–B10.

Here, we used the data from the model electrode charged to 4.2 V at a current rate of 12 mA cm^{-2} (Fig. 1 (A)). In accordance with the results of the model selection for the modified ONMF, we separated the 2D-XAS data into ten clusters by using the k-means method (see Fig. 6).

To quantitatively compare results obtained with the modified ONMF and with the k-

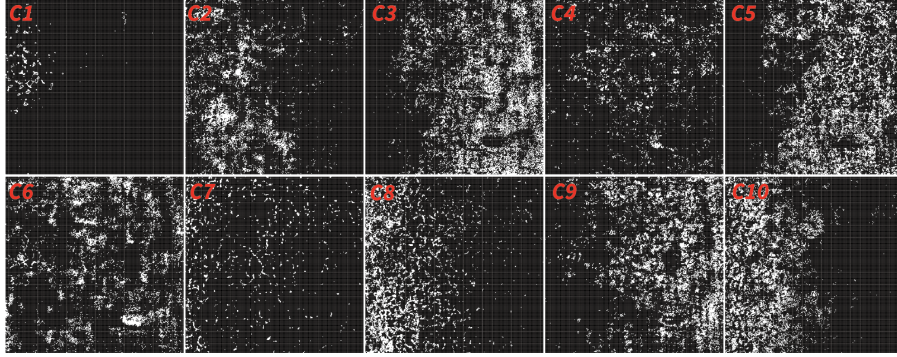


FIG. 6: Extraction of ten spatial domains C1–C10 using k-means method from real 2D-XAS data of model electrode charged to 4.2 V at a current rate of $12 \text{ mAc}\text{m}^{-2}$ in Fig. 1(A).

TABLE I: Cross correlation matrix of domain patterns extracted with modified ONMF and k-means method. Each element is a cross correlation between each of B1–B10 in Fig. 4(B) and each of C1–C10 in Fig. 6.

	C1	C2	C3	C4	C5	C6	C7	C8	C9	C10
B1	0.80	0.11	0.03	0.08	0.05	0.06	0.02	0.10	0.00	0.01
B2	0.03	0.61	0.07	0.18	0.03	0.03	0.02	0.22	0.01	0.28
B3	0.01	0.09	0.59	0.33	0.05	0.02	0.01	0.03	0.24	0.04
B4	0.07	0.05	0.07	0.53	0.03	0.03	0.01	0.00	0.25	0.07
B5	0.00	0.12	0.12	0.02	0.56	0.06	0.01	0.12	0.14	0.14
B6	0.02	0.03	0.07	0.01	0.16	0.55	0.08	0.00	0.31	0.01
B7	0.08	0.04	0.03	0.01	0.09	0.07	0.54	0.32	0.01	0.03
B8	0.01	0.04	0.05	0.01	0.07	0.13	0.28	0.48	0.01	0.32
B9	0.06	0.02	0.08	0.02	0.04	0.37	0.10	0.21	0.34	0.13
B10	0.02	0.12	0.31	0.16	0.32	0.07	0.05	0.09	0.15	0.08

means method, we calculated the cross correlation of the domain patterns extracted by both methods. Table I shows the cross correlation matrix between B1–B10 in Fig. 4(B) and C1–C10 in Fig. 6. The domain patterns B1–B8 obtained with the modified ONMF were highly correlated with C1–C8 obtained with the k-means method. Thus, the results of the methods are consistent.

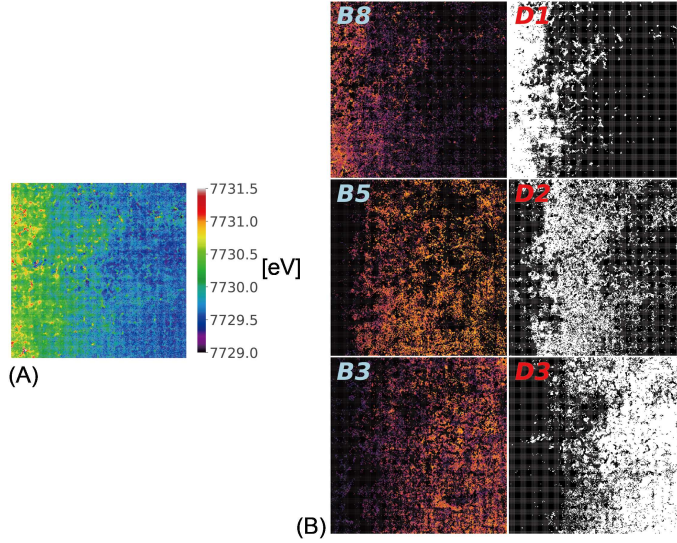


FIG. 7: Comparison of spatial domain patterns obtained with modified ONMF and with respect to the peak top energy. (A) Two-dimensional map of the peak top energy for model electrode charged to 4.2 V at a current rate of 12 mA cm^{-2} in Fig. 1(A). (B) D1, D2, D3: Three sets of pixels classified with respect to the peak top energy by thresholds E_1 and E_2 . $E_1 = 7730.18[\text{eV}]$ and $E_2 = 7729.79[\text{eV}]$. B8, B5, B3: Three domain patterns of modified ONMF most highly correlated with D1, D2 and D3

TABLE II: Cross correlation matrix of domain patterns obtained with modified ONMF and with respect to peak top energy. Each element is a cross correlation between each of B1–B10 in Fig. 4 (B) and each of D1–D3 in Fig. 7.

	B1	B2	B3	B4	B5	B6	B7	B8	B9	B10
D1	0.21	0.51	0.03	0.08	0.09	0.05	0.38	0.61	0.21	0.10
D2	0.10	0.26	0.12	0.12	0.34	0.18	0.14	0.15	0.17	0.25
D3	0.08	0.07	0.59	0.31	0.38	0.45	0.06	0.05	0.28	0.40

D. Comparison with spatial domain patterns with respect to peak top energy

Nakamura et al. obtained two-dimensional maps of SOC of Li_xCoO_2 in the model composite electrode from the peak top energy of the X-ray absorption spectrum at each pixel [17]. To confirm the consistency between these results and those obtained with the modified

TABLE III: Peak top energies (PTE) of spectra B1–B10 in Fig. 4 (C)

	PTE [eV]		PTE [eV]		PTE [eV]
B1	7730.17	B5	7729.79	B9	7729.84
B2	7730.18	B6	7729.71	B10	7729.75
B3	7729.65	B7	7730.24		
B4	7729.69	B8	7730.38		

ONMF, we compared the spatial domains obtained with the two methods.

Figure 7 (A) shows a two-dimensional map of the peak top energy obtained from the data on the electrode model charged to 4.2 V at a current rate of 12 mAcm⁻² in Fig. 1(A). As described in Subsection II.F, three sets of pixels, D1, D2 and D3, into which the pixels were classified with respect to the peak top energy by thresholds E_1 and E_2 , are plotted in Fig. 7(B). B8, B5, and B3 of Fig. 7(B) are the domains of the modified ONMF that are most highly correlated with D1, D2 and D3. Here, the thresholds maximizing the correlations between the domain patterns of the two methods are $E_1 = 7730.18$ [eV] and $E_2 = 7729.79$ [eV]. Table II is the cross correlation matrix of B1–B10 in Fig. 4(B) and D1–D3 in Fig. 7(B). The correlation coefficients between B8 and D1, between B5 and D2, and between B3 and D3 were 0.61, 0.34 and 0.59, respectively.

Furthermore, to confirm the consistency between domains obtained with the modified ONMF and with respect to the peak top energy, we also compared the relative relations of the peak top energies of the three domains B8, B5 and B3 most highly correlated with D1, D2 and D3 for thresholds E_1 and E_2 . The peak top energies of the spectra of B1–B10 in Fig. 4 are listed in Table III. The peak top energy of domain B8, 7730.38[eV], was higher than $E_1 = 7730.18$ [eV], while the peak top energy of domain B3, 7729.65[eV], was lower than $E_2 = 7729.79$ [eV]. However, the peak top energy of domain B5, 7729.79[eV], was not between E_1 and E_2 . Thus, the peak top energies of the domains extracted by the modified ONMF were partially correlated with the peak top energies of the domains obtained with respect to the peak top energy of the X-ray absorption spectra at the lower and higher sides of the peak top energy.

IV. DISCUSSION

A. Summary and conclusion

The automatic domain extraction method that we developed can identify and separate very small differences in X-ray absorption spectra. We removed the common background signal from 2D-XAS data of the model composite electrode by subtracting X-ray absorption spectrum of $\text{Li}_{0.5}\text{CoO}_2$ reference material from the 2D-XAS data; then we applied the modified ONMF to the difference spectra without the common background signal.

We assessed the performance of our proposed method on synthetic data that mimic profiles of X-ray absorption spectra. Bi-cross validation was used to show that number of the ground-truth domains was correctly identified and the spatial domains obtained by our method were identical with the ground-truth domains in the synthetic data (see Figs. 2 and 3). Next, we assessed the performance of our method on two different real 2D-XAS datasets (see Figs. 1(A) and (B)). We confirmed that our method could determine the rank of the factor matrices r and extract spatial domains with different spectral profiles from these data (see Figs. 4 and 5). Then, we quantitatively compared results obtained with our method and with the k-means method on the real 2D-XAS data shown in Figs. 1(A). We confirmed that almost all of the domain patterns obtained with our method were highly correlated with the results obtained with the k-means method (see Figs. 4(B) and 6 and Table I), and thus, results of the two methods were consistent. Finally, we quantitatively compared results obtained with our method and with respect to the peak top energy on real 2D-XAS data shown in Figs. 1(A). We confirmed that the spatial patterns and the peak top energies of the domains extracted by the modified ONMF were partially correlated with those of the domains obtained with respect to the lower and higher sides of the peak energy of the X-ray absorption spectra (see Fig. 7 and Tables II and III). Note that the consistency with results of the k-means method and the peak top energy had also been confirmed using other data clipped from a non-active region in Fig. 1(A) [38].

These results lead us to conclude that the modified ONMF in combination with removal of the common background signal can extract spatial domains with different spectral profiles from 2D-XAS data showing very little variation from one position to another. Moreover, we can conclude that domain patterns extracted by our method are invariant to methods of

classification and at least some of the domains represent physically interpretable information on the SOC.

B. Advantage over k-means method

As shown in Fig. 6 and Table I, we demonstrated that the k-means method can also automatically extract spatial domains with different profiles of absorption spectra from the 2D-XAS data of the model composite electrode. Our method has the following advantages over the k-means method:

1. The classification of the k-means method is sensitive to the amplitude of each element of data, whereas the classification of the NMF is invariant to the amplitude of each element of data because the amplitude of each element is incorporated into the factor matrix \mathbf{W} . Thus, our method can achieve scale-invariant separation of the X-ray absorption spectra from the reference X-ray absorption spectrum of $\text{Li}_{0.5}\text{CoO}_2$.
2. The domain patterns obtained with the k-means method are not allowed to overlap others, whereas the domain patterns obtained with our method are gently allowed to overlap others because of the column orthogonality imposed on \mathbf{W} by using the Lagrange multiplier method (Eq. (8)). Thus, our method can extract spatially overlapped domains.

C. Combination with Bayesian spectroscopy

X-ray absorption spectra can provide not only the SOC but also other information on local structures on the atomic scale, electron spin states, and so on [18–22]. Thus, after decomposing the 2D-XAS data into spatial domains and their corresponding spectra, we can examine the physical properties and features from the separated X-ray absorption spectra of the individual domains. For example, it is possible to use Bayesian spectroscopy on the separated absorption spectra [33–35] and extract the physical properties and features of the individual domains. If we integrated the separated spatial domains and their physical properties and features, we would gain a better understanding of the physical factors governing electrochemical reaction inhomogeneity.

V. ACKNOWLEDGMENTS

This work is supported by JST CREST (No. JPMJCR1861).

- [1] V. Etacheri, R. Marom, R. Elazari, G. Salitra, and D. Aurbach, *Energy & Environmental Science* **4**, 3243 (2011).
- [2] J. W. Fergus, *Journal of Power Sources* **195**, 939 (2010).
- [3] K. S. Kang, Y. S. Meng, J. Breger, C. P. Grey, and G. Ceder, *Science* **311**, 977 (2006).
- [4] R. Moshtev and B. Johnson, *Journal of Power Sources* **91**, 86 (2000).
- [5] B. Yan, C. Lim, L. L. Yin, and L. K. Zhu, *Journal of the Electrochemical Society* **159**, A1604 (2012).
- [6] T. Nishi, H. Nakai, and A. Kita, *Journal of the Electrochemical Society* **160**, A1785 (2013).
- [7] M. Katayama, K. Sumiwaka, R. Miyahara, H. Yamashige, H. Arai, Y. Uchimoto, T. Ohta, Y. Inada, and Z. Ogumi, *Journal of Power Sources* **269**, 994 (2014).
- [8] G. Ouvrard, M. Zerrouki, P. Soudan, B. Lestriez, C. Masquelier, M. Morcrette, S. Hamelet, S. Belin, A. M. Flank, and F. Baudelet, *Journal of Power Sources* **229**, 16 (2013).
- [9] W. C. Chueh, F. El Gabaly, J. D. Sugar, N. C. Bartelt, A. H. McDaniel, K. R. Fenton, K. R. Zavadil, T. Tyliszczak, W. Lai, and K. F. McCarty, *Nano Letters* **13**, 866 (2013).
- [10] L. Laffont, C. Delacourt, P. Gibot, M. Y. Wu, P. Kooyman, C. Masquelier, and J. M. Tarascon, *Chemistry of Materials* **18**, 5520 (2006).
- [11] C. Delmas, M. Maccario, L. Croguennec, F. Le Cras, and F. Weill, *Nature Materials* **7**, 665 (2008).
- [12] Y. Orikasa, T. Maeda, Y. Koyama, H. Murayama, K. Fukuda, H. Tanida, H. Arai, E. Matsubara, Y. Uchimoto, and Z. Ogumi, *Journal of the American Chemical Society* **135**, 5497 (2013).
- [13] J. Liu, M. Kunz, K. Chen, N. Tamura, and T. J. Richardson, *Journal of Physical Chemistry Letters* **1**, 2120 (2010).
- [14] H. Murayama, K. Kitada, K. Fukuda, A. Mitsui, K. Ohara, H. Arai, Y. Uchimoto, Z. Ogumi, and E. Matsubara, *Journal of Physical Chemistry C* **118**, 20750 (2014).
- [15] S. J. Harris, A. Timmons, D. R. Baker, and C. Monroe, *Chemical Physics Letters* **485**, 265 (2010).
- [16] T. Nakamura, T. Watanabe, K. Amezawa, H. Tanida, K. Ohara, Y. Uchimoto, and Z. Ogumi, *Solid State Ionics* **262**, 66 (2014).

- [17] T. Nakamura, T. Watanabe, Y. Kimura, K. Amezawa, K. Nitta, H. Tanida, K. Ohara, Y. Uchimoto, and Z. Ogumi, *Journal of Physical Chemistry C* **121**, 2118 (2017).
- [18] M. Wilke, F. Farges, P. E. Petit, G. E. Brown, and F. Martin, *American Mineralogist* **86**, 714 (2001).
- [19] P. Carra, B. T. Thole, M. Altarelli, and X. D. Wang, *Physical Review Letters* **70**, 694 (1993).
- [20] C. T. Chen, Y. U. Idzerda, H. J. Lin, N. V. Smith, G. Meigs, E. Chaban, G. H. Ho, E. Pellegrin, and F. Sette, *Physical Review Letters* **75**, 152 (1995).
- [21] J. Stöhr, *NEXAFS spectroscopy*, Springer series in surface sciences (Springer-Verlag, Berlin ; New York, 1992).
- [22] B. K. Teo, *EXAFS: Basic Principles and Data Analysis*, Inorganic Chemistry Concepts, (Springer Berlin Heidelberg, Berlin, Heidelberg, 1986).
- [23] D. D. Lee and H. S. Seung, *Nature* **401**, 788 (1999).
- [24] M. Shiga, K. Tatsumi, S. Muto, K. Tsuda, Y. Yamamoto, T. Mori, and T. Tanji, *Ultramicroscopy* **170**, 43 (2016).
- [25] M. Shiga and S. Muto, *E-Journal of Surface Science and Nanotechnology* **17**, 148 (2019).
- [26] Y. Nomura, K. Yamamoto, T. Hirayama, M. Ohkawa, E. Igaki, N. Hojo, and K. Saitoh, *Nano Lett* **18**, 5892 (2018).
- [27] A. Baliyan and H. Imai, *Sci Rep* **9**, 18241 (2019).
- [28] Y. Nomura, K. Yamamoto, T. Hirayama, E. Igaki, and K. Saitoh, *ACS Energy Letters* **5**, 2098 (2020).
- [29] R. Maruyama, K. Maeda, H. Moroda, I. Kato, M. Inoue, H. Miyakawa, and T. Aonishi, *Neural Netw* **55**, 11 (2014).
- [30] Z. Li, X. D. Wu, and H. Peng, *Pattern Recognition Letters* **31**, 905 (2010).
- [31] K. Kimura, Y. Tanaka, and M. Kudo, in *Proceedings of the Sixth Asian Conference on Machine Learning*, edited by P. Dinh and L. Hang (PMLR, 2014), vol. 39, pp. 129–141.
- [32] A. B. Owen and P. O. Perry, *Annals of Applied Statistics* **3**, 564 (2009).
- [33] K. Nagata, S. Sugita, and M. Okada, *Neural Networks* **28**, 82 (2012).
- [34] I. Akai, I. Kazunori, and O. Masato, *Journal of Physics* **1036**, 012022 (2018).
- [35] K. Iwamitsu, M. Okada, and I. Akai, *12th International Conference on Excitonic and Photonic Processes in Condensed Matter and Nano Materials (Excon 2018)* **1220** (2019).
- [36] A. Cichocki and A. H. Phan, *Ieice Transactions on Fundamentals of Electronics Communications and Computer Sciences* **E92-A**, 1279 (2009).

tions and Computer Sciences **E92a**, 708 (2009).

[37] C. M. Bishop, *Pattern recognition and machine learning*, Information science and statistics (Springer, New York, 2006).

[38] H. Tanimoto, M. Mizumaki, Y. Seno, I. Akai, and T. Aonishi, IEICE Tech. Rep. **119**, 113 (2020), ISSN 0913-5685.